



1. Introduction

In recent years, electrochemical technologies have played a key role in searching for reusable energy sources, including water splitting, fuel cells, and metal-air batteries to drive the development of clean and sustainable energy storage and conversion [1,2]. Rechargeable Zinc-air batteries (ZAB) have been extensively studied due to their high theoretical energy density, low cost, and environmental friendliness [3,4]. It is essential to develop cost-effective and durable electrocatalysts with high ORR and OER electrocatalytic activities for advanced ZAB [3,5]. However, the slow kinetics of OER and ORR impede excessively high electric potentials and low energy efficiency: $O_2 + 2H_2O + 4e^- \leftrightarrow 4OH^-$ [6]. Currently, batch mark OER and ORR catalysts used for ZAB are based on precious metals (Pt, Ru, and Ir) that have high costs and scarcity greatly limiting their large-scale commercial applications [7,8]. Therefore, it is of great significance to develop non-noble metal-based bifunctional electrocatalysts with high efficiency and durability for Zn-air batteries.

At present, the main challenge in catalyst design is to achieve versatility while maintaining high bifunctional catalytic activity at a low cost [9,10]. Alternative non-precious metal bifunctional oxygen electrocatalysts have been developed as Zn air cathodes, including metal-free carbon matrix composites, transition metal oxides [11,12], sulfides [13,14], and phosphides [15,16]. Among these electrocatalysts, cobalt-based transition metal-nitrogen-carbon (Co–N–C) composites are preferred owing to their low cost, excellent activity, and good stability [17,18]. However, it is difficult to prepare well-defined metal-nitrogen co-doped carbon catalysts due to the aggregation of metal atoms at high temperatures during the synthesis [19,20] that places of interest in low-temperature synthesis. Nevertheless, synthesizing ORR catalysts with high activity at a mild temperature is often very challenging [11,21]. In addition, other cobalt-based materials, such as cobalt oxides [22,23], cobalt sulfides [13,24], and cobalt phosphides [15,25] also have been studied, but suffer from poor catalytic activity and stability attributable to the alkaline corrosion during battery operation. Therefore, fabricating a single function Co-based catalyst with an ORR or OER is a relatively easier process owing to the less complicity. Nevertheless, there are still a few reports on high-performance cobalt-based catalysts with dual-functionalities [26,27]. For instance, Yu et al [28] described Co nano-islands rooted on Co–N–C nano-sheets derived from electrodeposition with outstanding bifunctional property for ZAB. The ZAB showed a small charge–discharge voltage ($0.82@10 \text{ mA cm}^{-2}$), high energy density (132 mW cm^{-2}), and outstanding durability. The DFT studies revealed that the synergy between Co metal particles and Co-N species is responsible for the high performance. However, it would be very difficult to keep the Co at the metallic state due to the very low oxidation potential. Especially when the Co is in the nano-form, the Co particles will be oxidized immediately in the air and it could cause a safety hazard, as the result the catalyst conductivity will be reduced so as the catalytic performance. In summary, catalyst aggregation and stability are the bottlenecks remaining unresolved in the field. Recent studies show that the cobalt nitride (Co_xN) possesses a unique advantage resulted from the Co-N bonding including better electron conductivity and good alkaline stability [29,30].

In the light of the above studies, we propose a novel strategy to synthesize a self-supporting $CoN-N_d$ nanosheet array on carbon

cloth (CC) as a bifunctional oxygen electrocatalyst through a facile hydrothermal process and - thermal nitridation treatment- NH_3 gas was used as a nitrogen source and annealed at a low temperature to ensure that the nanosheet structure of the catalyst remains intact during the post-annealing process. The activity of the catalyst was greatly promoted due to the high conversion of Co into CoN and the abundant N atom defect sites in the material. The optimized $CoN-N_d-300$ acts as an efficient bifunctional catalyst with high activity and outstanding durability toward both ORR and OER in alkaline solution (All potentials was calibrated to RHE, Fig. S1). The rechargeable ZAB using $CoN-N_d$ as an air cathode showed a small potential voltage ($0.79@10 \text{ mA cm}^{-2}$), a high power density (120 mW cm^{-2}), and robust durability up to 260 cycles. This work provides guiding strategies for the construction of bifunctional electrocatalysts.

2. Experimental section

2.1. M

Cobalt(II) acetate tetrahydrate ($C_4H_6CoO_4 \cdot 4H_2O$, 99.5%), Polyvinylpyrrolidone (PVP, K29, MW:58000), P_{123} (MW: 8400), F_{127} (MW: 12600), Ethylene glycol ($C_2H_6O_2$, AR), Methanol anhydrous (CH_3OH , AR 99.5%) were analytical reagent and used without further purification. Commercial Pt/C (20 wt% for platinum) was purchased from Alfa Aesar. RuO_2 powder is synthesized by directly calcining $RuCl_3$ in the air at $400^\circ C$.

2.2. C LDH/CC

200 mg of Cobalt (II) acetate tetrahydrate and 400 mg of PVP were dissolved in 7.5 mL of ethylene glycol under stirring. Then, 22.5 mL of methanol was added to the above solution and under vigorous stirring for 0.5 h. A piece of carbon cloth (CC, $1 \text{ cm} \times 4 \text{ cm}$) was ultrasonically cleaned in 0.5 M H_2SO_4 , deionized water, and ethanol for 15 min to remove impurities, respectively. Then the solution was transferred into a 50 mL Teflon-lined stainless steel autoclave containing the pretreated CC and kept at $120^\circ C$ for 12 h. After the autoclave cooled down slowly at room temperature, the resulting pink CC was taken out and further washed three times with ethanol and dried under vacuum at $60^\circ C$.

For comparison, PVP was replaced with an equivalent amount of F_{127} or P_{123} during the synthesis process.

2.3. C N/CC

The obtained Co LDH/CC was placed in a tube furnace and annealed at $200^\circ C$, $300^\circ C$, and $400^\circ C$ for 3 h with a ramp rate of $5^\circ C \text{ min}^{-1}$ under a flow of ammonia gas, respectively. The obtained sample was denoted as $CoN/CC-200$, $CoN-N_d/CC-300$, and $CoN/CC-400$, respectively. Note: N_d denotes N defect.

2.4. C N-C CH

We use the previous synthesis method to synthesize CoCH, only replacing NF with carbon cloth (CC) [31]. The obtained sample is then annealed in an ammonia atmosphere of $300^\circ C$ using the same nitriding method described above.

2.5. ZIF 67-N₃₀₀

ZIF 67 was synthesized using previous laboratory synthesis methods [32]. Then the obtained sample is annealed in an ammonia atmosphere of 300 °C using the same nitriding method described above.

2.6. Zn-air battery

The homemade Zn-air battery was assembled according to the following process: the air electrode was made by loading catalyst ink onto the carbon paper substrate (loading: 1 mg cm⁻²). The catalyst ink was prepared by mixing electrocatalysts with 5% Nafion solution and water/isopropanol solution (1:3 (v/v)). 6 M KOH and 0.2 M Zn(Ac)₂ were served as electrolytes. Then a polished zinc plate was used as the anode. As a comparison, Pt/C + RuO₂ mixed catalyst ink was prepared in the same procedure with a mass ratio of 1:1. All electrochemical tests were conducted on an electrochemical workstation (CHI 760E) under ambient conditions. The stability was tested by using the LAND battery testing system (BT2016A) at a current density of 5 mA cm⁻² with 20 min per cycle (10 min charge and 10 min discharge). The specific capacity was calculated from the following equation:

$$\text{Specific capacity} = \frac{Q}{w} \times 1000$$

3. Results and discussion

The synthetic processes of the CoN-N_d/CC are illustrated in Fig. 1a. The solvothermal method was used to prepare Co LDH nanosheet arrays grown in situ on carbon cloth (CC). Then, the precursor Co LDH is transformed into CoN-N_d nanosheets composed of nanoparticles by thermal ammonia treatment. The SEM image of Fig. 1b shows that a smooth CC surface before the growth of Co LDH species. After Co LDH is deposited, an interconnected sheet-like nanoarray is formed (Fig. 1c). After ammonia treatment at different temperatures, the morphologies of the Co_xN series are consistent with these of the Co LDH precursors (Fig. 1d and Fig. S2). The abundant gaps between the array-like structures facilitate the transport and release of electrolytes and gases, thereby improving catalytic performance.

The precursors and the corresponding ammonia-treatment products at different temperatures were analyzed by X-ray diffraction (XRD). After heating the Co LDH/CC under NH₃ atmosphere at different temperatures (200–400 °C), the Co LDH nanosheets were converted to Co_xN nanosheets. However, there is a significant discrepancy in the crystal structure of the obtained Co_xN at the different annealing temperatures. Fig. 2a shows the XRD pattern of the Co LDH precursor, which shows that the precursor has high crystallinity. For comparison, Fig. 2b–d shows the XRD patterns of the ammonia-treatment products. In Fig. 2b, the diffraction peak located near 42.2° corresponds to the crystal plane of CoN (200), while the other diffraction peaks correspond to the (001), (003), (006), and (110) crystal planes of Co LDH, respectively. It shows that CoN-200 is not completely nitridated at a temperature of 200 °C. The diffraction peaks of the annealed sample at 300 °C are positioned at around 36.2, 42.2, 61.3, 73.3, and 76.8° corresponding to (111), (200), (220), (311), and (222) crystal planes of CoN (JCPDS: 16–0116), respectively [33,34]. Moreover, no diffraction peaks of precursors and impurities were observed, suggesting a complete phase conversion from precursor to CoN at 300 °C (Fig. 2c). The diffraction peaks in the sample revealed the coexistence of CoN and Co_{0.547}N (JCPDS: 41–0943) in CoN-400 (Fig. 2d), after further annealing at 400 °C [35]. The above XRD

analysis indicate that the crystal structure of Co_xN nanosheets can be adjusted by changing the annealing temperature, which provides an opportunity to evaluate the catalytic activities of Co_xN with different crystal phases.

Moreover, the influences of different surfactants on the CoN crystallinity and morphology were also investigated. As depicted in Fig. S3, the obtained Co LDH-s (s = PVP, F₁₂₇, P₁₂₃) and the series of CoN-s have similar crystal structures. However, there are palpable differences in the micromorphology of CoN-s (Fig. S4). SEM images show that CoN-P₁₂₃ and CoN-F₁₂₇ have granular and stacked sheet-shaped structures, respectively, while the interconnected sheet-like nanoarrays presented by CoN-PVP are more propitious to electrolyte diffusion and gas emission, thus contributing to better electrocatalytic activity (Fig. S5).

Besides, we further discussed the nitrogen treatment products of different cobalt-based precursors at 300 °C under an ammonia atmosphere. XRD patterns found that only some of the orthorhombic Co(CO₃)_{0.5}(OH)·0.11H₂O (CoCH) was converted to CoN, while the crystal structure of ZIF-67 material hardly changed (Figs. S6–a–c). These results indicate that only Co LDH can be converted completely to CoN by treatment in an ammonia atmosphere at 300 °C, and shows better OER performance than other control materials (Fig. S6d). The study found that the differences in the morphology (Fig. S7), composition and crystal structure of CoN-CoCH and ZIF-67-N₃₀₀ are the key factors maximizing the results of ammonia treatment.

Furthermore, the nitrogen adsorption–desorption isotherms of the series of CoN-N_d (Scraped off the CC) show a typical type-IV behavior (Fig. 2e). Among all samples, the CoN-N_d-300 nanosheets have the largest Brunauer–Emmett–Teller (BET) surface area (74.3 m² g⁻¹), which is higher than those of Co LDH (18.4 m² g⁻¹), CoN-200 (24.0 m² g⁻¹), and CoN-400 (24.3 m² g⁻¹) nanosheets. The average BJH pore diameters of Co LDH, CoN-200, CoN-N_d-300, and CoN-400 are 3.3, 3.9, 3.7, and 3.9 nm, respectively (Figs. S8a–c). This change may be due to the different crystalline forms of CoN at different ammonia-treatment temperatures, thus showing different porosity. The high porosity of CoN-N_d-300 facilitates the mass transfer and exposes more active sites, which greatly promotes electrocatalytic performance [36,37].

Electron paramagnetic resonance (EPR) spectra were employed to determine the formation of defects (Fig. 2f). A broad signal (at 2.088) can be assigned to the contribution from unpaired electrons, indicating N defects exist in the CoN-N_d [31,38,39]. It can be found that the signal intensity of CoN-N_d-300 is significantly higher than those of Co LDH nanosheets, CoN-200 and CoN-400, indicating that the array-like CoN-N_d-300 has a higher degree of defects. The studies confirmed that the N defects create free electrons resulting in higher conductivity and additional active sites, thereby increasing the catalytic activity [38,40]. In addition, as shown in Fig. S9, the HRTEM image of CoN-N_d revealed many discontinuities presenting in the lattice fringes (marked with red dashed circles), indicating that there are abundant defects in CoN-N_d. These results indicate that the ammoniate temperature of 300 °C is the optimal condition for the formation of abundant nitrogen defects.

Transmission electron microscopy (TEM) is used to study the structural features of the CoN/CC. Fig. 3a shows that the CoN-N_d nanosheets are composed of nanoparticles with an average particle size of ~10 nm. The selected area electron diffraction (SAED) mode (Fig. 3b) shows the diffraction spots of CoN (111), (220) and (311) [40]. The HR-TEM image presents three types of lattice fringes (Fig. 3c), corresponding to the interplanar spacings of 0.248 nm (111), 0.151 nm (220), and 0.214 nm (200) of the cubic CoN crystal plane, respectively, corroborating the successful synthesis of CoN crystal [40]. Notably, the HRTEM images of CoN-N_d have many discontinuity points (marked by a white dotted circle), indicating the presence of a defect-rich structure on the base

surface. A locally disordered arrangement of atoms causes a large number of defects on the substrate, and thus amorphous structures are observed in the catalyst, which leads to the formation of the secondary active sites [38,39]. Meanwhile, the high-angle annular dark field (HAADF) TEM element mapping shows that Co and N are uniformly distributed throughout the CoN-N_d/CC (Fig. 3d), further demonstrating the CoN-N_d nanosheet formation.

X-ray photoelectron spectroscopy (XPS) was used to detect the chemical states of surface elements in CoN-x synthesized at different temperatures. The XPS survey spectrum reveals the presence of Co, N, C, and O elements in all samples (Fig. S10a). Three typical peaks at 284.0, 284.8, and 286.0 eV observed in C 1s spectra are deconvoluted to C=C, C-C, and C-O as a

calibration standard (Fig. S10b) [32,41]. By examining the hydrothermal sample as shown in Fig. S10c, the Co 2p_{3/2} spectral deconvolution of Co LDH nanosheets can be performed as three components locating at 780.7, 782.2 and 786 eV, belonging to the Co³⁺, Co²⁺, and satellite peaks, respectively, which are consistent with two kinds of coordination environments of Co species in Co LDH [42,43]. Meanwhile, a weak single peak of pyrrolic-N was found in the high-resolution N 1s of Co LDH due to a small number of PVP molecules adsorbed on the surface of the sample

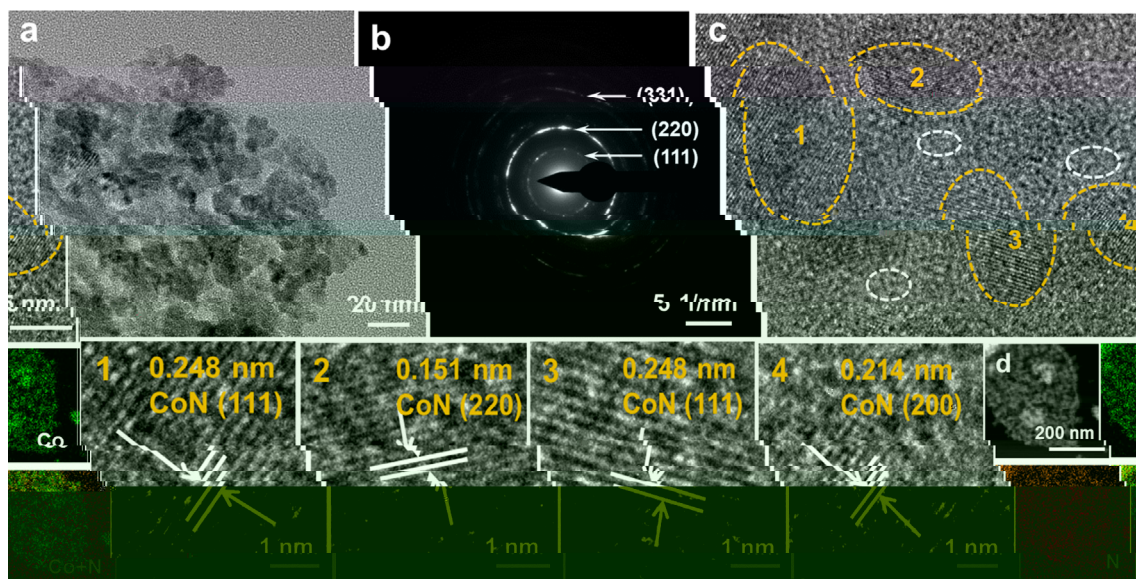


Fig. 3. (a) TEM image, (b) SAED and (c) High-Resolution TEM images, and (d) HAADF-STEM image and corresponding elemental mappings of CoN-N_d/CC (color online).

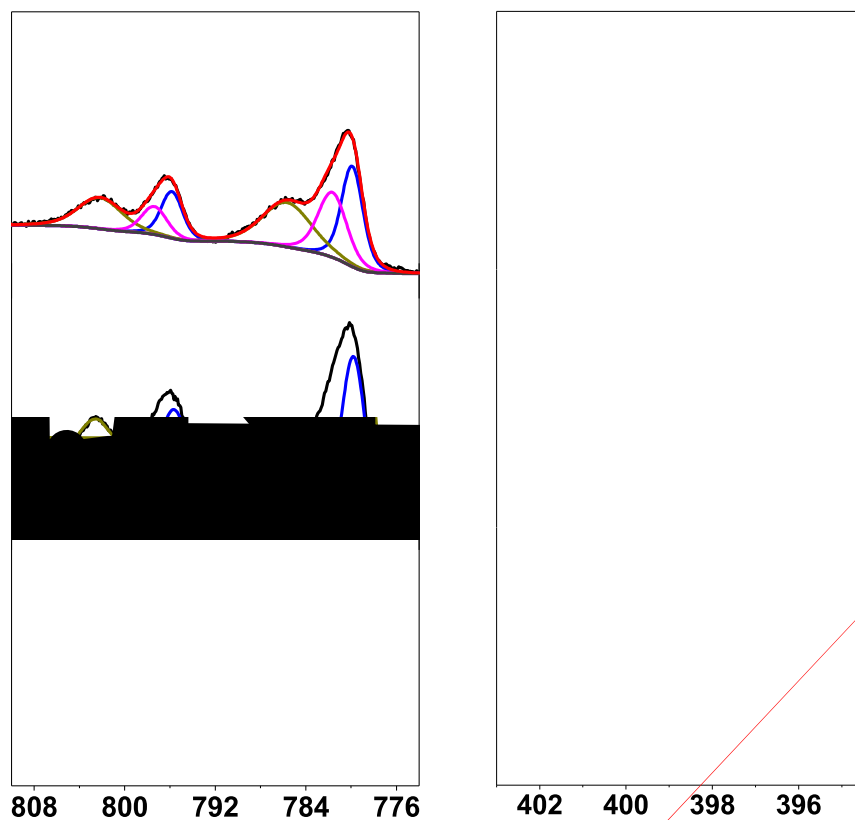
the peaks at 779.9 and 781.9 eV for Co 2_{3/2} indicate the chemical features of Co³⁺ and Co²⁺. Anecdotally, the percentage of Co³⁺ gradually increases with the rise of nitriding temperature (Fig. 4a). Fig. 4b illustrates the XPS spectrum of N 1s for CoN-x. The high-resolution N 1s spectrum of CoN-N_d-300 indicates that the peak of N-Co located at 398.2 eV was observed in addition to the N-H surface terminal group from NH₃ treatment [45,46]. Moreover, compared with CoN-200 and 400, when the nitriding temperature was 300 °C, the relative peak strength of Co-N was the strongest and the surface percentage was as high as 89.1%, indicating that the condition of 300 °C was most favorable for the formation of Co-N bond.

The OER behavior of the catalysts was measured by using a standard three-electrode system in 1.0 M KOH at a scan rate of 2 mV s⁻¹. Fig. 5a shows the current density of CoN-N_d-300 catalyst increases rapidly with potential, indicating the excellent OER performance. A significant effect of the N-defect was presented itself in OER performance, where the CoN-N_d-300 demands a lower overpotential of 243 mV to reach the current density of 10 mA cm⁻². It is much lower than those of Co LDH (243 mV), CoN-200 (291 mV), CoN-400 (310 mV), and RuO₂ (257 mV), and most recently reported electrocatalysts (Table S1). Another critical reaction of OER electrocatalytic activity is the small Tafel slope. As shown in Fig. 5b, the Tafel slope of 70.8 mV dec⁻¹ for CoN-N_d-300 is smaller than those of Co LDH (74.6 mV dec⁻¹), CoN-200 (74.0 mV dec⁻¹), CoN-400 (75.8 mV dec⁻¹), and RuO₂ (73.3 mV dec⁻¹), suggesting faster reaction kinetics [32]. To further elucidate the intrinsic mechanism for the enhancement of OER activity, per-site turnover frequency (TOF) is employed to compare the practical performance of catalysts. The TOF value is calculated based on the assumption that all metal atoms are active sites, and the number of metal atoms is obtained by ICP-AES (Table S2) [47]. The potential-dependent TOF curve of CoN-N_d-300 catalyst shows the enhanced intrinsic activity per site compared to Co LDH, CoN-200, and CoN-400 (Fig. 5c). As expected, the CoN-N_d-300 catalyst possesses the largest electrochemically active surface area (ECSA) of 6208 cm² (normalized per cm² of electrode area), which is much higher than those of Co LDH (4386 cm²), CoN-200 (4328 cm²), and CoN-400 (1121 cm²) (Table S3).

Electrochemical impedance spectroscopy (EIS) (Fig. 5d) shows that CoN-N_d-300 has the smallest charge transfer resistance (*R*_{ct})

than others, verifying that CoN-N_d-300 catalyst exhibits a faster electron transfer rate during the electrocatalytic OER process. Generally, the electrochemical double-layer capacity (*C*_{dl}) is directly proportional to the ECSA. The *C*_{dl} value can be calculated using cyclic voltammetry (CV) curves in the non-Faradaic region (Fig. S11) [48]. As shown in Fig. 5e, the *C*_{dl} values of CoN-N_d-300 is 372.5 mF cm⁻², which is significantly higher than those of Co LDH (263.2 mF cm⁻²), CoN-200 (259.7 mF cm⁻²), and CoN-400 (67.3 mF cm⁻²), indicating more active sites in CoN-N_d/CC-300. Noticeably, using CoN-N_d/CC-300 as the working electrode, the durability of the catalyst was probed through constant current electrolysis at 100 mA cm⁻² for 100 h (Fig. 5f). The stability of the catalyst deteriorates slightly over time, which may be caused by the change of the microstructure (Fig. S12) and the surface chemical state (Fig. S13). Nevertheless, the CoN-N_d/CC-300 showed way better stability as compare to Pt/C (Fig. 6f).

The electrocatalytic performance of CoN-N_d for ORR was assessed by rotating disk electrode (RDE) and rotating ring disk electrode (RRDE) methods in 0.1 M KOH electrolyte. Fig. 6a depicted the CV curves of CoN and Pt/C in O₂ and N₂-saturated 0.1 M KOH solution. CoN showed a well-defined cathodic peak at about 0.78 V vs. RHE comparable to Pt/C, indicating the favorable ORR catalytic activity. The LSV curves and Tafel slopes of CoN-N_d and Pt/C were shown in Fig. 6b, c. The half-wave potential (*E*_{1/2}) of CoN-N_d (0.77 V) was only 0.07 V lower than that of Pt/C (0.84 V), while its limit current density (*J*_L = 5.2 mA cm⁻²) was 0.3 V higher than that of Pt/C (*J*_L = 4.9 mA cm⁻²), and the Tafel slope was comparable to Pt/C [49]. Simultaneously, CoN-N_d showed a smaller charge transfer resistance compared to Pt/C (Fig. S14), illustrating CoN-N_d possesses a faster charge transfer rate [26]. The above results suggested that the robust ORR activity of CoN-N_d. To further understand the reaction mechanism, the LSV curves were recorded at different rotational speeds from 400 to 2025 rpm (Fig. S15a). The obtained Koutecky-Levich (K-L) diagram revealed an excellent linear relationship within the potential range of 0.3–0.6 V vs RHE, indicating that the number of electrons transferred per oxygen molecule was the same in the ORR process (Fig. S15b) [50]. Besides, the H₂O₂ yield of CoN was less than 15% and the electron transfer number (*n*) was ~4 in the potential range of 0.2–0.8 V, which further proves the four-electron process of ORR (Fig. 6d). The potential difference (ΔE) between *E*_{1/2} of ORR and



overpotential at 10 mA cm^{-2} (η_{10}) of OER was generally used to evaluate the overall bifunctional activity of the catalyst. The smaller ΔE value indicates the higher bifunctional activity [51]. As presented in Fig. 6e, the ΔE of CoN-N_d (0.79 V) was equivalent to Pt/C + RuO₂ (0.78 V), which illustrates that CoN-N_d possesses outstanding bifunctional activity. CV testing was performed in a

mixed solution of 5 mM K₃[Fe(CN)₆] and 0.1 M KCl with different scan rates to evaluate ECSA of CoN-N_d. As shown in Fig. S16, there is a good linear relationship between the peak current and scan rate, which indicates that CoN-N_d has a large ECSA [52,53]. SCN⁻ was used as a probe to verify the role of CoN-N_d during ORR because SCN⁻ poison the M-N_x site [53]. The current density of



- Co₃O₄ nanosheets boost oxygen electrocatalysis bifunctionality for advanced Zn-air batteries, *Energy Storage Mater.* 32 (2020) 20–29.
- [23] D. Ding, K. Shen, X. Chen, H. Chen, J. Chen, T. Fan, R. Wu, Y. Li, Multi-Level Architecture Optimization of MOF-Templated Co-Based Nanoparticles Embedded in Hollow N-Doped Carbon Polyhedra for Efficient OER and ORR, *ACS Catal.* 8 (9) (2018) 7879–7888.
- [24] J. Yin, Y. Li, F. Lv, M. Lu, K. Sun, W. Wang, L. Wang, F. Cheng, Y. Li, P. Xi, S. Guo, Oxygen Vacancies Dominated NiS₂/CoS₂ Interface Porous Nanowires for Portable Zn-Air Batteries Driven Water Splitting Devices, *Adv. Mater.* 29 (2017) 1704681.
- [25] Y. Guo, P. Yuan, J. Zhang, H. Xia, F. Cheng, M. Zhou, J. Li, Y. Qiao, S. Mu, Q. Xu, Co₂P-CoN Double Active Centers Confined in N-Doped Carbon Nanotube: Heterostructural Engineering for Trifunctional Catalysis toward HER, ORR, OER, and Zn-Air Batteries Driven Water Splitting, *Adv. Funct. Mater.* 28 (2018) 1805641.
- [26] J. Zhu, J. Fan, T. Cheng, M. Cao, Z. Sun, R. Zhou, L. Huang, D. Wang, Y. Li, Y. Wu, Bilayer nanosheets of unusual stoichiometric bismuth oxychloride for potassium ion storage and CO₂ reduction, *Nano Energy* 75 (2020) 104939.
- [27] W. Zhu, L. Zhang, S. Liu, A. Li, X. Yuan, C. Hu, G. Zhang, W. Deng, K. Zang, J. Luo, Y. Zhu, M. Gu, Z.-J. Zhao, J. Gong, Enhanced CO₂ Electroreduction on Neighboring Zn/Co Monomers by Electronic Effect, *Angew. Chem. Int. Ed.* 59 (31) (2020) 12664–12668.
- [28] P. Yu, L. Wang, F. Sun, Y. Xie, X. Liu, J. Ma, X. Wang, C. Tian, J. Li, H. Fu, Co Nanoislands Rooted on Co-N-C Nanosheets as Efficient Oxygen Electrocatalyst for Zn-Air Batteries, *Adv. Mater.* 31 (2019) 1901666.
- [29] F. Xie, X. Cao, F. Qu, A.M. Asiri, X. Sun, Cobalt nitride nanowire array as an efficient electrochemical sensor for glucose and H₂O₂ detection, *Sensor. Actuat. B-Chem.* 255 (2018) 1254–1261.
- [30] F. Meng, H. Zhong, D.i. Bao, J. Yan, X. Zhang, In Situ Coupling of Strung Co₄N and Intertwined N-C Fibers toward Free-Standing Bifunctional Cathode for Robust, Efficient, and Flexible Zn-Air Batteries, *J. Am. Chem. Soc.* 138 (32) (2016) 10226–10231.
- [31] X. Huang, X. Xu, X. Luan, D. Cheng, CoP nanowires coupled with CoMoP nanosheets as a highly efficient cooperative catalyst for hydrogen evolution reaction, *Nano Energy* 68 (2020) 104332.
- [32] P. Yan, M. Huang, B. Wang, Z. Wan, M. Qian, H.u. Yan, T.T. Isimjan, J. Tian, X. Yang, Oxygen defect-rich double-layer hierarchical porous Co₃O₄ arrays as high-efficient oxygen evolution catalyst for overall water splitting, *J. Energy Chem.* 47 (2020) 299–306.
- [33] L. Hu, Y. Hu, R. Liu, Y. Mao, M.-S. Balogun, Y. Tong, Co-based MOF-derived Co/CoN/Co₂P ternary composite embedded in N- and P-doped carbon as bifunctional nanocatalysts for efficient overall water splitting, *Int. J. Hydrogen Energy* 44 (23) (2019) 11402–11410.
- [34] C. Ray, S.C. Lee, B. Jin, A. Kundu, J.H. Park, S. Chan Jun, Chan Jun, Conceptual design of three-dimensional CoN/Ni₃N-coupled nanograsses integrated on N-doped carbon to serve as efficient and robust water splitting electrocatalysts, *J. Mater. Chem. A* 6 (10) (2018) 4466–4476.
- [35] Z. Chen, Y. Ha, Y. Liu, H. Wang, H. Yang, H. Xu, Y. Li, R. Wu, In Situ Formation of Cobalt Nitrides/Graphitic Carbon Composites as Efficient Bifunctional Electrocatalysts for Overall Water Splitting, *ACS Appl. Mater. Interfaces* 10 (8) (2018) 7134–7144.
- [36] P. Karfa, K.C. Majhi, R. Madhuri, Shape-Dependent Electrocatalytic Activity of Iridium Oxide Decorated Erbium Pyrosilicate toward the Hydrogen Evolution Reaction over the Entire pH Range, *ACS Catal.* 8 (9) (2018) 8830–8843.
- [37] T. Zhou, H. Shan, H. Yu, C. Zhong, J. Ge, N. Zhang, W. Chu, W. Yan, Q. Xu, H. Wu, C. Wu, Y. Xie, Nanopore Confinement of Electrocatalysts Optimizing Triple Transport for an Ultrahigh-Power-Density Zinc-Air Fuel Cell with Robust Stability, *Adv. Mater.* 32 (47) (2020) 2003251, <https://doi.org/10.1002/adma.202003251>.
- [38] Z. Zhang, J. Hao, W. Yang, J. Tang, Defect-Rich CoP/Nitrogen-Doped Carbon Composites Derived from a Metal-Organic Framework: High-Performance Electrocatalysts for the Hydrogen Evolution Reaction, *ChemCatChem* 7 (2015) 1920–1925.
- [39] N.Q. Tran, B.K. Kang, M.H. Woo, D.H. Yoon, Enrichment of Pyrrolic Nitrogen by Hole Defects in Nitrogen and Sulfur Co-Doped Graphene Hydrogel for Flexible Supercapacitors, *ChemSusChem* 9 (16) (2016) 2261–2268.
- [40] Z. Xue, J. Kang, D. Guo, C. Zhu, C. Li, X. Zhang, Y. Chen, Self-supported cobalt nitride porous nanowire arrays as bifunctional electrocatalyst for overall water splitting, *Electrochim. Acta* 273 (2018) 229–238.
- [41] H. Zhang, D.J. Hagen, X. Li, A. Graff, F. Heyroth, B. Fuhrmann, I. Kostanovskiy, S. L. Schweizer, F. Caddeo, A.W. Maijenburg, S. Parkin, R.B. Wehrspohn, Atomic Layer Deposition of Cobalt Phosphide for Efficient Water Splitting, *Angew. Chem. Int. Ed.* 59 (39) (2020) 17172–17176.
- [42] Q. Chen, R. Ding, H. Liu, L. Zhou, Y.i. Wang, Y. Zhang, G. Fan, Flexible Active-Site Engineering of Monometallic Co-Layered Double Hydroxides for Achieving High-Performance Bifunctional Electrocatalyst toward Oxygen Evolution and H₂O₂ Reduction, *ACS Appl. Mater. Interfaces* 12 (11) (2020) 12919–12929.
- [43] Y. Lin, H. Wang, C.-K. Peng, L. Bu, C.-L. Chiang, K. Tian, Y. Zhao, J. Zhao, Y.-G. Lin, J.-M. Lee, L. Gao, Co-Induced Electronic Optimization of Hierarchical NiFe LDH for Oxygen Evolution, *Small* 16 (38) (2020) 2002426, <https://doi.org/10.1002/sml.202002426>.
- [44] F. Song, W. Li, J. Yang, G. Han, T. Yan, X.i. Liu, Y.i. Rao, P. Liao, Z. Cao, Y. Sun, Interfacial Sites between Cobalt Nitride and Cobalt Act as Bifunctional Catalysts for Hydrogen Electrochemistry, *ACS Energy Lett.* 4 (7) (2019) 1594–1601.
- [45] Y. Yang, R. Zeng, Y. Xiong, F.J. DiSalvo, H.D. Abruña, Cobalt-Based Nitride-Core Oxide-Shell Oxygen Reduction Electrocatalysts, *J. Am. Chem. Soc.* 141 (49) (2019) 19241–19245.
- [46] R.-Q. Li, X.-Y. Wan, B.-L. Chen, R.-Y. Cao, Q.-H. Ji, J. Deng, K.-G. Qu, X.-B. Wang, Y.-C. Zhu, Hierarchical Ni₃N/Ni_{0.8}Mo_{0.8}N heterostructure nanorods arrays as efficient electrocatalysts for overall water and urea electrolysis, *Chem. Eng. J.* 409 (2021) 128240.
- [47] B. Wang, H. Huang, M. Huang, P. Yan, T.T. Isimjan, X. Yang, Electron-transfer enhanced MoO₂-Ni heterostructures as a highly efficient pH-universal catalyst for hydrogen evolution, *Sci. China Chem.* 63 (6) (2020) 841–849.
- [48] B. Wang, H. Huang, T. Sun, P. Yan, T.T. Isimjan, J. Tian, X. Yang, Dissolution reconstruction of electron-transfer enhanced hierarchical NiS_x-MoO₂ nanosponges as a promising industrialized hydrogen evolution catalyst beyond Pt/C, *J. Colloid Interface Sci.* 567 (2020) 339–346.
- [49] A.I. Douka, Y. Xu, H. Yang, S. Zaman, Y. Yan, H. Liu, M.A. Salam, B.Y. Xia, A Zeolitic-Imidazole Frameworks-Derived Interconnected Macroporous Carbon Matrix for Efficient Oxygen Electrocatalysis in Rechargeable Zinc-Air Batteries, *Adv. Mater.* 32 (2020) 2002170.
- [50] X. Cheng, S. Dou, G. Qin, B. Wang, P. Yan, T.T. Isimjan, X. Yang, Rational design of highly selective nitrogen-doped Fe₂O₃-CNTs catalyst towards H₂O₂ generation in alkaline media, *Int. J. Hydrogen Energy* 45 (11) (2020) 6128–6137.
- [51] Y. Niu, X. Teng, S. Gong, Z. Chen, A bimetallic alloy anchored on biomass-derived porous N-doped carbon fibers as a self-supporting bifunctional oxygen electrocatalyst for flexible Zn-air batteries, *J. Mater. Chem. A* 8 (27) (2020) 13725–13734.
- [52] M. Qian, X. Cheng, T. Sun, J. Tian, T.T. Isimjan, Z. Shi, X. Yang, Synergistic catalytic effect of N-doped carbon embedded with CoFe-rich CoFe₂O₄ clusters as highly efficient catalyst towards oxygen reduction, *J. Alloy. Compd.* 819 (2020) 153015.
- [53] M. Qian, M. Xu, S. Zhou, J. Tian, T. Taylor Isimjan, Z. Shi, X. Yang, Template synthesis of two-dimensional ternary nickel-cobalt-nitrogen co-doped porous carbon film: Promoting the conductivity and more active sites for oxygen reduction, *J. Colloid Interface Sci.* 564 (2020) 276–285.
- [54] Y.-J. Wu, X.-H. Wu, T.-X. Tu, P.-F. Zhang, J.-T. Li, Y. Zhou, L. Huang, S.-G. Sun, Controlled synthesis of FeN_x-CoN_x dual active sites interfaced with metallic Co nanoparticles as bifunctional oxygen electrocatalysts for rechargeable Zn-air batteries, *Appl. Catal. B: Environ.* 278 (2020) 119259.
- [55] S. Ramakrishnan, J. Balamurugan, M. Vinothkannan, A.R. Kim, S. Sengodan, D.J. Yoo, Nitrogen-doped graphene encapsulated FeCoMoS nanoparticles as advanced trifunctional catalyst for water splitting devices and zinc-air batteries, *Appl. Catal. B: Environ.* 279 (2020) 119381.
- [56] Z. Zhang, X. Zhao, S. Xi, L. Zhang, Z. Chen, Z. Zeng, M. Huang, H. Yang, B. Liu, S.J. Pennycook, P. Chen, Atomically Dispersed Cobalt Trifunctional Electrocatalysts with Tailored Coordination Environment for Flexible Rechargeable Zn-Air Battery and Self-Driven Water Splitting, *Adv. Energy Mater.* 10 (2020) 2002896.